Area x-ray detector based on a lens-coupled charge-coupled device

Mark W. Tate
Physics Department, Laboratory of Atomic and Solid State Physics, Cornell University, Ithaca, New York 14853-2501

Darol Chamberlain
Cornell High Energy Synchrotron Source (CHESS), Cornell University, Ithaca, New York 14853-8001

Sol M. Gruner[a)]
Physics Department, Laboratory of Atomic and Solid State Physics, Cornell University, Ithaca, New York 14853-2501 and Cornell High Energy Synchrotron Source (CHESS), Cornell University, Ithaca, New York 14853-8001

(Received 23 March 2005; accepted 5 June 2005; published online 4 August 2005)

An area x-ray detector constructed using commercially available "off-the-shelf" parts is described and its performance is characterized. The detector consists of a 1024×1024 pixel charge-coupled device (CCD) camera optically coupled to x-ray sensitive phosphor screen using a standard 35 mm camera lens. The conversion efficiency, spatial nonuniformity, spatial resolution and the detective quantum efficiency of the detector have been measured. Also shown is an example of data taken with the detector. The detector is a relatively low-cost device suitable for a wide variety of quantitative x-ray experiments where the input area need not be larger than about 70 mm across. [DOI: 10.1063/1.2001307]

I. INTRODUCTION

Area detectors must meet a variety of technical requirements to be suitable tools for x-ray applications. Detector requirements include adequate input area, spatial resolution, dynamic range, signal-to-noise ratio (S/N), and sufficient stability to allow the device to hold a calibration for a reasonable period of time. Charge-coupled device (CCD) x-ray detectors are available from a number of manufacturers, but are typically quite expensive. The objective of this study is to evaluate the level of performance attainable using a simple lens-coupled CCD detector designed around commercially available components. It complements other simple CCD x-ray detector designs that have been described in the literature.[1–5] One should also note that detectors using large, custom lens systems in conjunction with very large format CCDs are under development.[6]

The CCDs in the current generation of x-ray detectors are usually optically coupled to an x-ray sensitive phosphor screen by either a fiber-optic taper or a lens.[7–10] Fiber-optic tapers generally provide a more efficient way of reducing the optical image of the phosphor screen on to the CCD.[11] A fiber-optic taper will typically have much more variation on a fine scale than a lens due to the structure of the fibers and defects in their packing. This is most noticeable at the fiber-optic bundle interfaces, resulting in a fixed "chicken wire" pattern. Most importantly, the taper has to be optically coupled to the CCD without unduly compromising the overall efficiency or spatial resolution. Additionally, this optical bond must withstand the thermal stresses incurred at the low operating temperatures required for low noise imaging. The most commonly used method is to directly bond the taper to the CCD with an optical coupling compound, such as a clear optical epoxy. Larger CCDs require a compliant bond that will mitigate the stress due to thermal mismatch. Bonding is a difficult step that requires experience and specialized equipment and entails considerable risk to an expensive CCD. The difficulty of this last coupling step has deterred many x-ray scientists from making their own CCD detectors.

Lenses provide a simpler way of optically coupling the phosphor and the CCD. Many CCD cameras offer adapters for most common 35 mm camera lenses, further simplifying the process. Lens coupling often comes at the price of a lower light coupling efficiency, especially in a demagnifying geometry as would be typical in most x-ray scattering detectors. In addition, one must deal with a host of aberrations that degrade optimal performance. These aberrations may include coma, geometric distortions, and vignetting, as well as the lens having a nonplanar surface of best focus. The low f-number lenses which are desirable in this application for light collection efficiency make correction for aberrations even harder. Modern aspheric lenses minimize these aberrations greatly, but the large number of lens elements required to obtain good correction results in many reflective surfaces that contribute to lens flare, effectively limiting the single frame dynamic range.

Note that most 35 mm camera lenses are designed to offer best correction when focused at infinity. Lenses intended for copy work where the object plane must be flat typically are $f/4$ and slower, which is much too slow for this application. Several lenses were evaluated in this study, with different lenses being preferable in certain situations.

Although we have considerable experience with fabricat-

[a)]Author to whom correspondence should be addressed; electronic mail: smg26@cornell.edu

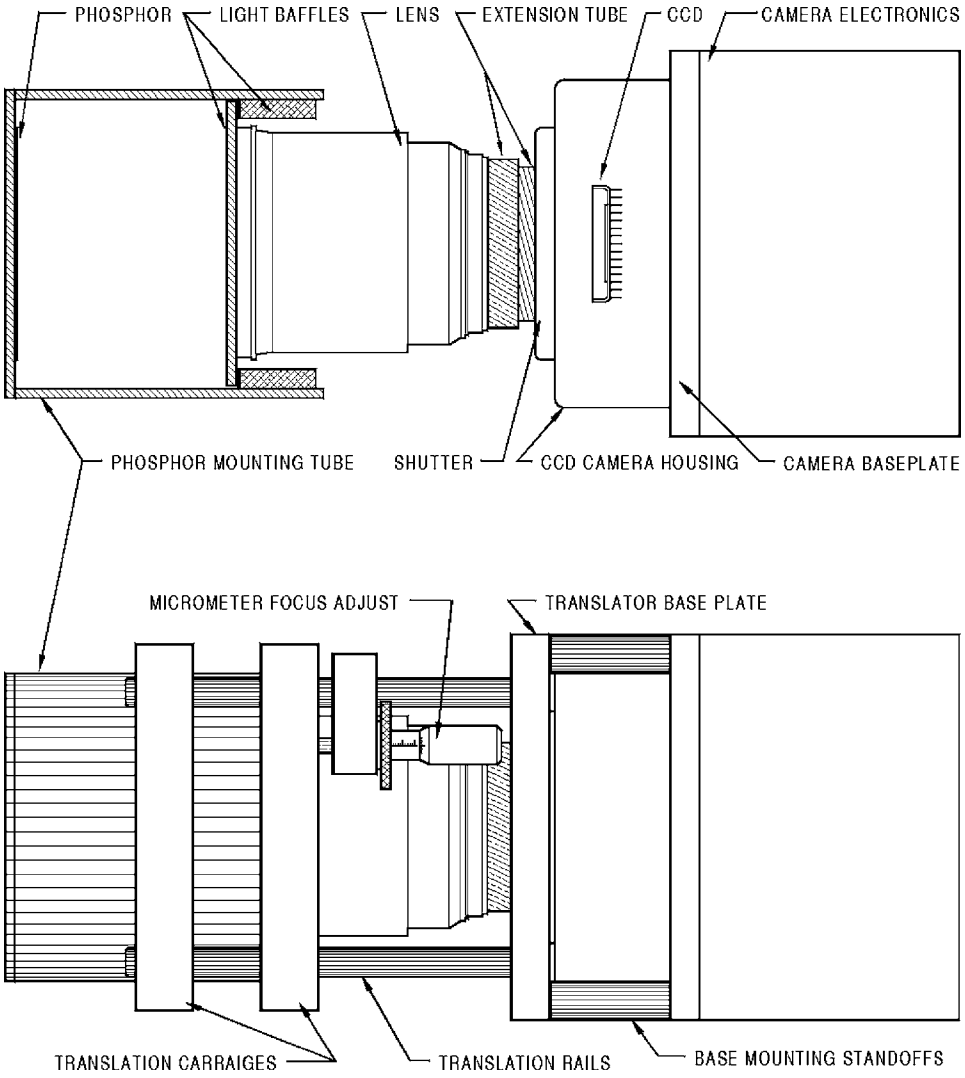

FIG. 1. Detector schematic. The top portion of the figure shows a cutaway view of the detector. The x-ray image, converted to visible light in the phosphor screen, is projected onto the CCD via a camera lens. The extension tube adjusts the distance from the lens to the CCD, allowing the image magnification factor to be changed. The CCD is contained within a hermetically sealed camera housing and cooled via a thermoelectric module (not shown). The bottom portion of the figure shows the mechanical fixture that supports the phosphor mounting tube from the CCD camera baseplate. This fixture allows micrometer adjustment of the phosphor position relative to the camera in order to achieve best focus. The detector assembly is approximately 30 cm in length when using the Sigma $f/1.8$ lens.

ing fiber-optically coupled CCD detectors,[12–17] we recognize that the requisite coupling procedures are not easily performed. This study was a response to a question we are frequently asked: Is there a relatively simple and inexpensive CCD detector that can be assembled out of commercially available parts by a typical academic x-ray physics laboratory? As seen below, a good quality detector can, indeed, be so fabricated.

II. DETECTOR CONSTRUCTION

In making an efficient x-ray detector, one tries to optimize a number of factors relating to the imaging problem at hand. One usually begins with the quantized nature of the x-ray signal and the inherent Poisson statistics associated with that signal. To have a high overall quantum efficiency, the detector should have a high probability of recording a signal (greater than one electron) from every incident x ray. For an 8 keV x ray stopped in an efficient phosphor, roughly 400 visible photons will be emitted. The light collection efficiency of the lens, η_{lens}, goes as

$$\eta_{\text{lens}} = T_{\text{lens}}/[2f(1+m^{-1})]^2, \tag{1}$$

where T_{lens} is the transmission of the lens materials, f is the f number of the lens, and m is the lens magnification (m^{-1} is the demagnification).[18] The size of the CCD relative to the needed x-ray imaging area sets the image magnification (typically demagnifying for most scattering applications). Given that the CCD records at best 80% of the incident visible light, one would need a lens faster than $f/2$ if the image demagnification factor was $2.5\times$ (roughly 0.5% lens efficiency) to retain high quantum efficiency. With this constraint, one would then evaluate the system for other relevant parameters. For instance, to perform well at low dose per pixel, the recorded signal per x ray should be on the order of, (or above), the zero dose noise inherent in reading the CCD (which is often on the order of 10 electrons). Factors such as this will place further constraints on the imaging components.

A schematic drawing of the lens-based detector is shown in Fig. 1.[19] The detector consists of a thin phosphor sheet held in front of a camera lens followed by a Finger Lakes Instrumentation (FLI) IMG 1024S CCD camera (Finger Lakes Instrumentation, LLC, Lima, N.Y.). The phosphor used in the detector characterizations was a $Gd_2O_2S:Tb$(P43) phosphor (Thomas Electronics, Wayne, N.J.) that was deposited in our laboratory on a thin (65 μm) sheet of aluminized Mylar with a phosphor weight of 12.8 mg/cm^2.[20] Grain size was on the order of 2–8 μm. The

peak fluorescence of this phosphor is at 545 nm. The aluminized Mylar increases the light collected from the phosphor by reflecting efferent light back toward the camera. A similar P43 phosphor sheet with large particle coating on aluminized mylar was obtained from Grant Scientific Corporation (Gilbert, SC 29054) and yielded similar performance in the detector. The phosphor is held flat in a brass fixture behind an entrance window consisting of a 75 μm thick sheet of opaque black polyethelyne (taken from the packaging of Ilfospeed Multigrade II enlarging paper, Ilford Inc., Paramus, N.J.). The phosphor/window fixture in turn caps a brass cylinder (1/8 in. wall) that extends partially over the camera lens assembly, forming a portion of a light-tight shield. In addition, this cylinder is thick enough to absorb stray radiation (up to 50 keV x rays) that could otherwise exit the camera. A brass ring mounted onto the filter threads of the camera lens, and which fits closely to the inside of the cylinder, completes the light-tight enclosure. The cylinder, which can slide freely past the ring mounted on the lens, is held within a linear translation carriage that can slide along a set of four 3/8 in. diam rails mounted to the camera base. A micrometer attached to this carriage is used to finely adjust the distance between the phosphor and camera. The interior surfaces of the light-tight enclosure are painted with flat black paint to reduce reflected light.

Camera lenses from several different manufacturers were evaluated. A Canon EF 85 mm $f/1.2$ L USM lens (Canon USA, Lake Success, N.Y.) was evaluated for its low f number as was a Nikon Nikkor 35 mm $f/1.4$ lens (Nikon USA, Melville, N.Y.). A Sigma 24 mm $f/1.8$ EX Aspherical DG Macro Lens (Sigma Corp. of America, Ronkonkoma, N.Y.) was chosen for the combination of both relatively low f number and macro capability. The Canon and Sigma lenses have aspheric lens elements to reduce aberrations at low f number. The Nikon lens was from a vintage that predates the common use of aspherics in consumer lenses, although it should be noted that certain Nikon lenses now incorporate aspheric elements. The Nikon and Sigma lenses were mounted on a Nikon K3 bayonet F-mount adapter attached to a custom extension tube. The extension tube, constructed from two mating threaded cylinders, can be continuously varied in length, moving the lens relative to the CCD and thereby changing the image magnification. The extension tube attaches directly into the standard 2 in.-24 SC thread mount of the FLI camera housing. At its shortest length, the extension tube holds the lens at the standard position relative to the image plane. The Canon lens was mounted using a similarly threaded custom extension tube attached to the bayonet mounting ring taken from a Canon EF12 extension tube. Due to the longer focal length of the Canon lens, a longer phosphor mounting tube was needed in this case. Additional extension tubes (Nikon PK-11A or Canon EF12) were used to extend the range of possible magnifications of the lenses. The Canon lens was also tested with one and with two Canon 500D close up lens attachments. These lens attachments thread into the filter threads on the front of a lens, allowing closer focus by effectively changing the focal length of the lens.

A SITe SI-003AB 1024×1024 back-illuminated CCD (SITe, Tigard, Ore.) was chosen with the Finger Lakes Instruments camera due to its high quantum efficiency (80% at 545 nm) and large format (1024×1024 pixels, 24 μm in size). Both of these features serve to maximize recorded signal/x ray, but come with a premium in cost. Using a less expensive, front-illuminated CCD, typically will reduce the recorded signal/x ray by a factor of 2 or more. Note that the CCD size closely matches the imaging area for 35 mm film, meaning that a number of lenses are available for use in this system. An integral thermoelectric cooler maintains the temperature of the CCD at -35 °C to reduce dark current. The camera was ordered with the water-cooled option to allow lower temperature operation than the standard model. In addition, a xenon gas backfill of the sealed camera chamber was tried in place of the standard argon purge. This latter modification offered no real benefit since the minimum practical CCD operating temperature was found to be the point at which condensation formed on the optical window to the camera, a temperature obtainable with an argon purge. The cooling water temperature was limited to 15 °C by condensation considerations as well. The standard optical window (UV super HMC, Hoya Corporation USA, San Jose, CA) of the sealed camera is multicoated with an average transmission of 99.7%.

The Finger Lakes camera comes with the electronics and software needed to control and read the CCD. The integral optical shutter can be used to control exposure, but an additional external x-ray shutter is preferred to limit buildup of phosphor afterglow. Images are digitized to 16 bits per pixel and downloaded through a parallel port interface on the host computer at 50 K pixels/s (21 s for a full 1024×1024 image). Charge from one, two, or four adjacent pixels along each axis can be summed (binned) within the CCD before digitization. Increasing the binning both increases readout speed and reduces the total read noise at the cost of image resolution.

Drawings of the mechanical camera components are provided in the supplementary materials.[19]

III. DETECTOR PERFORMANCE

A variety of tests were made to characterize the performance of the detector. Table I provides a summary of the detector characteristics.

A. Sensitivity and uniformity of response

The electronic gain, g, of the amplifier chain was measured to be 3.6 e^-/analog-to-digital conversion units (ADU) using the photon transfer technique.[21] The pixel-to-pixel variance, σ_e^2, in a uniform image should be equal to the number of recorded quanta per pixel, N_e, when the shot noise is well above the read noise floor. In practice, one computes the variance in the difference of two nominally identical visible light images to remove inevitable fixed patterns due to variations in illumination or sensitivity. The intensity is taken for the sum of the images. Whereas the Poisson statistics depend on the number of fundamental quanta (electrons in the CCD), the intensity of these images is digitized in terms of

TABLE I. Detector characterization.

CCD	SITe SI-003AB
Pixel format	1024×1024
Optical reduction (magnification^{-1})	2.0–2.8
Active input area (mm^2)	49×49–69×69
Pixel size at phosphor (μm)	48–67
Phosphor	$Gd_2O_2S:Tb$(P43)
Phosphor thickness (mg/cm^2)	12.8
CCD operating temperature (°C)	−35
Analog-to-digital resolution (bits)	16
Gain (e^-/analog-to-digital unit)	3.6
Readout time (s)	21
Read noise (e^-/pixel) at zero x-ray dose (rms)	12
Full well (e^-/pixel)	3×10^5
Dark accumulation (e^-/pixel/s @ −35 °C)	0.30

ADU. The intensity in ADU, N_{ADU}, is related to the number of electrons by $N_e=gN_{\mathrm{ADU}}$. Likewise, the standard deviation measured in ADU, σ_{ADU}, is related by $\sigma_e=g\sigma_{\mathrm{ADU}}$. The gain is found simply by $g=N_{\mathrm{ADU}}/\sigma^2_{\mathrm{ADU}}$. The gain was measured with varying levels of illumination (10–70% of full well) and was found to be constant within 1%. The noise floor of the system measured at zero dose was found to be 12 e^- rms. Note that x-ray images cannot be used for this gain measurement procedure since multiple visible photons from a single x-ray conversion event are recorded and will be correlated, affecting the resulting statistical variations. This measurement requires an uncorrelated signal.

To measure sensitivity of the system, a source of known flux was used to illuminate the central portion of the phosphor. An efficient NaI scintilator was used to calibrate the flux coming through a 6 mm diam collimator from a ~10 mCi ^{55}Fe source (5.9 keV x rays). Results are summarized in Table II. As the demagnification is changed, sensitivity is seen to follow that expected in Eq. (1). For example, for the Sigma lens, as the demagnification goes from 2.12× to 2.57×, the sensitivity should drop by a factor of $(3.57/3.12)^2=1.31$ compared to the observed drop of 1.32×. As the f number is increased from the maximum aperture for a given lens, however, the drop in the sensitivity is less than expected. In addition, one would expect that the Canon lens would be more than twice as sensitive as the Sigma lens at a given optical reduction, say 2.5×, but it was found to be only 39% brighter. Note that the f number given by the manufacturer for a complex lens system does not represent the performance of the lens in all situations, but rather, the true performance will depend on lens placement and focus. Closeup lens attachments are known to improve the light throughput of the system as compared to extension tubes, as can be seen in the table. Note that no extension tube was needed for the Canon lens to reach focus at 2.22× with two 500D closeup attachments, and in fact, this combination is closer to the expected improvement due to the f number as compared to the Sigma lens at a similar magnification (which itself needed only a small extension).

One expects proportionately more light per x ray for x rays with higher energies. For 8 keV x rays, commonly used in laboratory sources, one would expect each of these lenses to record >2 e^-/x ray at demagnifications lower than 2.7×, yielding good quantum efficiency. With a read noise of 12 e^-, only a few x rays/pixel are needed to bring the S/N ratio above unity. Of course, the increased signal due to faster lenses or a lower demagnification will improve the low dose performance.

Uniformity of response was measured by illuminating the phosphor using a 50 W TFS-6050 Cu microfocus x-ray tube powered by a TCM-5000M power supply (TruFocus Corporation, Watsonville, Ca.). The source was held 1 m from the phosphor and was biased to 12 kV, producing a flood field measured to be uniform to less than 0.5% over the detector area. Table II shows the falloff at the edges and corners relative to the signal recorded in the center. Fast lenses typically show this behavior, which improves as the lens is stopped down to a higher f number. The Canon lens

TABLE II. Sensitivity and uniformity of response.

				Uniformity[b]	
Lens	f number	Demagnification	Sensitivity[a]	Edge	Corner
Sigma 24 mm f/1.8	1.8	2.12	2.02	0.81	0.64
	1.8	2.26	1.78	0.76	0.60
	1.8	2.57	1.53	0.77	0.62
	2.8	2.27	1.02	0.92	0.76
Canon 85 mm f/1.2	1.2	2.74	1.97	0.93	0.90
	1.2	2.49	2.20	0.94	0.89
with one closeup lens	1.2	2.60	2.90	0.93	0.80
with one closeup lens	1.2	2.08	3.70	0.94	0.83
with two closeup lenses	1.2	2.22	4.69	0.80	0.64
Nikon 35 mm f/1.4	1.4	2.27	2.78	0.84	0.68
	2.0	2.27	1.76	0.95	0.86
	2.8	2.27	0.94	0.97	0.94

[a]Measured at center of detector (e^-/5.9 keV x ray)
[b]Relative to center (center=1).

shows the least vignetting at wide aperture, although it becomes comparable with the other lenses with the addition of two closeup lens attachments. Note that it is routine practice with most area detectors to correct for nonuniformities of this magnitude via software.[22,23] However, the lower sensitivity in the corners will affect the S/N ratio at a given x-ray dose (see Sec. III D).

B. Spatial linearity (image distortion)

In addition to variations in coupling efficiency, lenses typically introduce barrel or pincushion distortions that must be corrected. Each lens and magnification will produce a unique spatial distortion that must be calibrated and removed via software. A 51 μm thick tungsten mask with a square lattice of lithographically formed 75 μm holes with a 1 mm pitch (Towne Technologies, Somerville, N.J.) was used to measure and correct this distortion.[22] The image of the illuminated mask was used to create an array of displacement vectors relative to an ideal square array without distortion. The displacement vector for each pixel was then obtained by interpolation between the displacement values of the adjacent mask holes.

A second, arbitrarily displaced exposure of the same mask can be used to verify the distortion-correction procedure. This second image is corrected using the displacement map produced from the first image. One can then compare the corrected image to an ideal grid. When using the Sigma $f/1.8$ lens at a demagnification of 2.38×, the corrected image produced an array of spots with an rms displacement of 0.08 pixels, with no spot deviating more than 0.72 pixels from its ideal location.

C. Spatial resolution

The spatial resolution of each of the lens systems was characterized using the spot mask used to measure image distortion as described above (Fig. 2). This test shows that the aspheric lens elements in the Sigma lens improves coma considerably [Fig. 2(a_2)]. The Nikon lens, which predates their updated aspheric lenses, has considerable coma [Fig. 2(b_2)] which improves noticeably at $f/2.8$ and higher. Coma for the Canon lens without closeup attachment was very noticeable [Fig. 2(c_2)], but improves with one and, still further, with two closeup lenses [Fig. 2(e_2)]. Finding a best focus for this last combination depends on the desired use of the system. Focusing at best full width half maximum (FWHM) produces a halo, at about 5% intensity, around each spot out to 0.5 mm [Fig. 2(d_1)]. This halo can be narrowed considerably, but with broader FWHM, by changing the position of focus by 1 mm [Fig. 2(e_1)]. Note that in this age of motorized lenses, Canon has chosen to remove manual control of aperture and focus (from an unpowered lens), so performance at other apertures were not evaluated. Undoubtedly, this lens would have much greater spatial resolution at higher f numbers.

The Sigma lens showed the highest and most consistent spatial resolution over the detector at full aperture, and we characterize it here more fully than the other lenses (measured at 2.38× reduction). Measurements of the point spread function (PSF) were made from isolated point illuminated spots along the detector diagonal at approximately 0, 11, 23, and 34 mm from the center. Values of PSF versus radius for each of the four positions on the detector are shown in Table III.

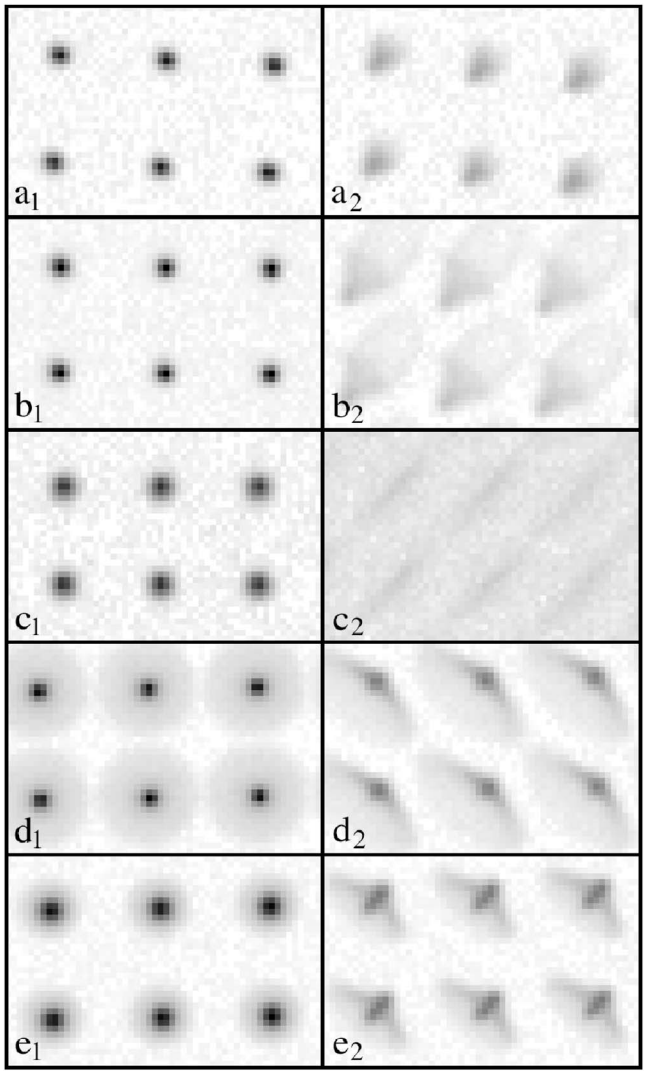

FIG. 2. Selected image areas (54×36 pixels) of point illumination of the detector through a 75 μm array of holes. Six of the holes, on a 1 mm pitch, are seen in each section. Images in the left column are taken from the central portion of the full image whereas the images in the right column are from the upper right corner. (a_1), (a_2) Central and upper right portions, respectively, of image using the Sigma $f/1.8$ lens at 2.26× demagnification. The comet-tail spreading of the spots in (a_2) is indicative of coma in the lens system. (b_1), (b_2) Images from the detector using the Nikon $f/1.4$ lens at 2.27× demagnification. Considerably more coma is seen compared to the Sigma lens. (c_1), (c_2) Images from the detector using the Canon $f/1.2$ lens at 2.49× demagnification. While the spots in the central region are sharp, the coma in the corners has spread the signal almost uniformly between the 1 mm spaced spots. (d_1), (d_2) Images from the detector using the Canon $f/1.2$ lens in conjunction with 2 Canon 500D closeup attachments at 2.22× demagnification. The central portion shows narrow spot surrounded by a wide halo spreading at the level of several percent. Coma has improved considerably from that in (c_2). (e_1), (e_2) Images taken using the lens configuration of (d_1) but with a 1 mm shift in the position of the phosphor plane. Note the spread of the spots at low level in (e_1) has reduced from that in (d_1), but the FWHM is greater.

Lens coupling always involves a compromise between efficiency and image fidelity. Faster lenses (e.g., small f

TABLE III. Point spread function.[a]

Distance from center (mm)	0	11	23	34
Full width at half-maximum (μm)	125	115	125	175
Full width at 1/10 maximum (μm)	230	210	240	320
Full width at 1/100 maximum (μm)	360	340	380	500
Full width at 1/1000 maximum (μm)	550	520	570	740
Full width at 1/10 000 maximum (μm)	1250	1400	1300	1450

[a]Sigma $f/1.8$ lens at 2.38× demagnification.

numbers) are more efficient in capturing the phosphor light, thereby improving sensitivity, but at the cost of greater variation in the quality of the center-to-edge imaging fidelity. The amount of light spreading for a given distance from the center depends on the focusing of the lens. This lens is corrected to work at macro distances, but does not have an entirely flat object plane. The actual focus along the axis of the lens is slightly past the phosphor, with the best focus of the phosphor plane coming on a ring about 11 mm from the center. Focusing in this manner minimizes the total distortion over the widest possible area (one could choose to have the best focus at the center with even poorer focus at the edges). The spreading of the spots at the center is slightly greater than at 11 mm. The spots farthest from the center of the detector show the most spreading, with significant coma developing in the outer radial positions [Fig. $2(a_2)$]. Except for the corners, the PSF found for this lens is only slightly larger than that found for a fiber-optically coupled detector (80 μm FWHM and 450 μm full width 1/1000 maximum).[15]

Testing of the PSF to 10^{-4} may seem excessive for most imaging applications, but as the following will show, the spread of light at levels even less than 10^{-4} in the PSF can have an appreciable effect if many pixels in the image are illuminated.[11] In fact, one would need to know the PSF to at least 10^{-8} to determine the light spread to 1% contrast if the source comes from the light emanating from 10^6 pixels. Rather than extend the range of the PSF measurement, it is much easier to look for effects of the low level PSF from light spreading from an extended source. To test this, a flood exposure was made while covering half the area of the detector with a knife-edge mask. Signal spreading behind the knife edge is directly related to the low level PSF. Figure 3 shows normalized intensity versus distance from the knife edge for this lens coupled detector and a fiber-optically coupled detector constructed within our laboratory.[15] Whereas the PSF falls to 10^{-3} within 0.5 mm for the lens-coupled detector, a large illuminated field results in a slowly varying background (flare) to spread over the entire sensor. This flare was found to be remarkably independent of the lens used, the aperture setting, or the introduction of additional light baffling before or after the lens. Indeed, the quite uniform nature of this scatter indicates that the PSF flattens abruptly at the 10^{-8} level and extends to the edge of the detector.

Flare in lens systems is well known and results from reflections from the many interfaces. The most reflective surface in the optical path is, by far, the phosphor screen itself, which is a bright white polycrystalline layer. Given that the glass elements of the lens reflect on the order of several percent of the incident light (even with antireflection coatings), it is not surprising that one would have a diffuse secondary reflection coming from the phosphor screen that is on the order of 1%, given a large primary illuminated area. We were able to verify this as a major source of the flare by covering a small portion of the unilluminated area of the phosphor (lens side) with a piece of black paper and noting the dark, in-focus image of this paper in a repeat of the above test. A monolithic, transparent phosphor layer with an absorbing optical layer used in place of the aluminized mylar backing could potentially reduce this secondary reflection significantly, although at the cost of reduced sensitivity.

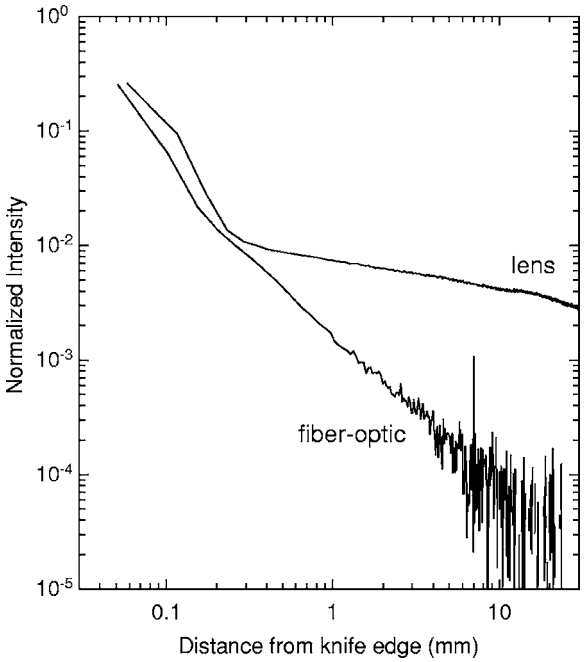

FIG. 3. Long range image flare from an extended source of illumination. Half the detector was placed under uniform x-ray illumination with the other half obstructed with a knife edge. Shown is the intensity of the signal spreading under the knife edge as a function of distance from the edge, both for this lens-coupled detector and a fiber-optically based detector constructed within our laboratory (see Ref. 15). Intensities are normalized to the intensity per pixel in the illuminated area. Both detectors exhibit similar behavior within 0.2 mm of the knife edge where the spread is dominated by the short length-scale point spread function. At longer length scales, the lens system shows a slowly varying scattering level on the order of one percent caused by reflections in the system. The spreading in the fiber-optic system comes from light scattering in the phosphor layer as well as incomplete absorption of light escaping the central cores of the optical fibers.

Light scattering in the fiber optic system falls much more rapidly, but is still limited by light spread within the fiber optics and phosphor. One should note that at the level seen in the lens system, one would be hard pressed to see this flare in film photography using this lens unless some region was grossly overexposed. It is only with the extended dynamic range of a cooled, scientific-grade CCD that it becomes readily apparent. This level of flare is within acceptable bounds for many x-ray imaging applications as seen below. There are, however, applications for which this lens-coupled system would probably not be appropriate, such as scattering experiments for which the shape of the scattering curve must be measured over several orders of magnitude in

intensity. The scattered light will also contribute a shot noise to the background, as well as limit the ultimate recorded contrast in the system.

D. Detective quantum efficiency

The detective quantum efficiency (DQE) of the detector is a measure of the actual noise of the recorded signal relative to the inherent noise,[24,25] and is given by

$$\mathrm{DQE} = \frac{(\mathrm{signal/noise})^2_{\mathrm{output}}}{(\mathrm{signal/noise})^2_{\mathrm{input}}}. \tag{2}$$

For an ideal detector, the DQE will be unity, with the noise solely determined by the Poisson statistics of the x-ray dose. Here, the inherent noise is equal to the square root of the number of incident x rays. Any detector limitations will be manifested by the lowering of the DQE from unity. The DQE will in general depend on variables such as the integrated x-ray dose, the size (or spatial frequency) of the x-ray feature, and the rate of accumulation.

The DQE versus dose was measured by taking a series of exposures through the 75 μm hole mask used to calibrate spatial distortions. By varying the exposure time (1–1000 s) and x-ray tube current, the average dose through each hole was varied between 60 and 3×10^5 x rays. Dose was calibrated using an efficient NaI scintillator. The x-ray tube was biased at 12 kV and 0.2–1.0 mA and was held 1 m from the hole mask. While not a monochromatic source, the average x-ray energy was determined to be roughly 8 keV with the tube biased at 12 kV. The sensitivity in the center of the detector was measured to be 2.0 e^-/x ray. These measurements were taken with the Sigma $f/1.8$ lens with a demagnification of 2.38×.

Accumulated dark current was subtracted from each image using an average of four zero-dose images of the appropriate exposure length. An average was used to reduce the noise contribution introduced in the subtraction process. Data were also corrected for intensity and spatial nonuniformities.[22] The intensity of each spot was computed by integrating an area within a radius of 3.4 pixels from the spot centroid (an area containing 37 pixels) and subtracting the background level found in a 9 pixel wide annulus outside of the spot. At doses less than 1000 x rays/spot, the noise was calculated from a single image by taking the standard deviation of the spot intensities in the 8 mm×8 mm local area. This calculation was repeated at different positions on the detector face. At higher dose, the fixed pattern variation in the mask hole sizes (roughly 3%) limits the statistics. One can remove the hole-size dependence by taking the difference of the spot intensities measured for the same hole in two independent frames. The noise can be found from the standard deviation of the pairwise differences in an 8 mm ×8 mm local area, whereas the measured signal is the mean of the intensities of the pairwise sum. Note that to test the true performance of the detector, the two images should be displaced relative to one another in order that limitations of the detector correction procedure can be seen.[15] Here we displace the detector 2 mm between measurements.

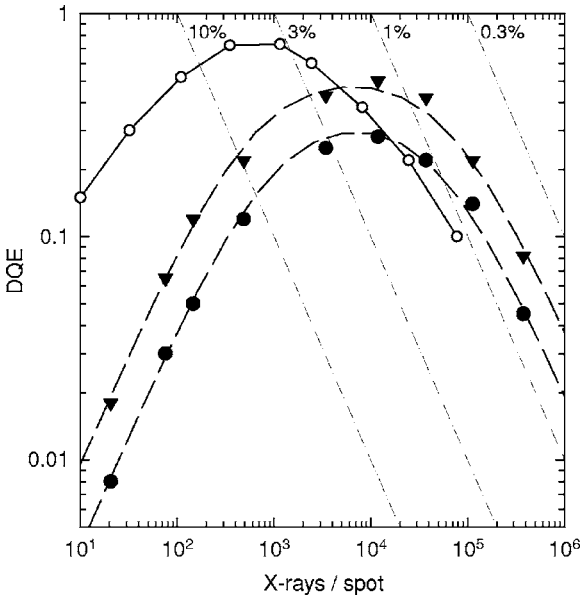

FIG. 4. DQE vs. dose for 75 μm spot illumination by 8 keV x rays in the center (inverted closed triangles) and near the corners (closed circles) of the detector. Data was obtained using the Sigma lens at 2.38:1 reduction. The dashed lines are fits to the data using a simple three parameter fit to the recorded noise in the image. The dash-dotted lines are lines of constant accuracy (noise/dose) at the levels indicated. A fixed system read noise limits the curves at low dose. Falloff at high dose, along lines of constant accuracy, is indicative of a fixed-pattern systematic noise. Also included is a curve obtained with a fiber-optic system (open circles) using the same test procedure (see Ref. 15).

The DQE versus dose, measured at both the center and the corners of the detector, is shown in Fig. 4. Also shown for comparison is the DQE curve for an efficient fiber-optic system obtained with the same experimental setup.[15] The three curves all follow the same general trends, increasing from low dose, reaching a maximum, and then falling again at high dose. This characteristic shape can be modeled with three detector-dependent noise sources. Consider the model in which the variance, $\sigma^2_{\mathrm{total}}$, in the measurement of an x-ray feature goes as

$$\sigma^2_{\mathrm{total}} = A^2 + N_{\mathrm{x\text{-}ray}}/B + (C \times N_{\mathrm{x\text{-}ray}})^2, \tag{3}$$

where $N_{\mathrm{x\text{-}ray}}$ is the number of incident x rays and A, B, and C are detector parameters relating to the read noise of the measurement, the quantum efficiency, and the limiting accuracy due to systematic fixed-pattern noise, respectively. The DQE in this model will be given by $N_{\mathrm{x\text{-}ray}}/\sigma^2_{\mathrm{total}}$. The dashed curves shown in Fig. 5 are fits to the data using this model.

At low dose, the constant A in Eq. (3) will dominate the variance and the DQE will increase linearly with dose. Recall that the digitization of each pixel value from the CCD has an associated 12 e^- rms noise. Subtracting the (averaged) background frame further increases the noise/pixel to 13.4 e^-. Since the integration area of each of the x-ray spots covers 37 pixels, the resulting noise per integration is increased by another factor of $\sqrt{37}$ to 82 e^-. The spatial distortion correction procedure acts as a nonuniform smoothing filter. Smoothing will reduce the noise within an area of interest by a factor that depends on the size and shape of that area as well as on the type of smoothing. Noise at zero dose

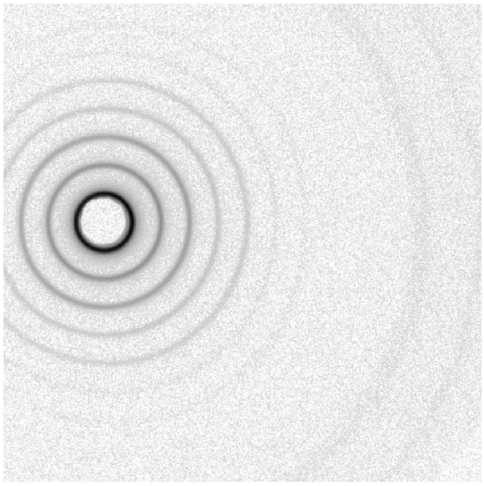

FIG. 5. Small angle powder diffraction from lamellar phase sample of silver stearate (lamellar spacing=4.868 nm). This one dimensional phase yields equally spaced, concentric diffraction rings. The beam in the center of the pattern is blocked by a circular beam stop. The first order ring is just outside the stop. The faint arcs on the right of the image are due to hydrocarbon chain packing in the direction transverse to the lamellar stacking. This image is the sum of seven 200 s exposures with a sample to detector distance of 10.4 cm. The image is displayed on a nonlinear scale to allow more of the diffraction features to be seen.

in uncorrected images for this size area was found to be 82 e^-, as expected, whereas the smoothing reduces the average noise in the same region to 62 e^-/spot. This yields an equivalent noise of 31 x rays/spot in the center of the detector and 47 x rays/spot in the corners (which is higher due to the decreased sensitivity per x ray there). The values fit to the DQE data of Fig. 4 yielded 32 and 49 x rays in the center and corners of the detector, respectively, in good agreement with the estimated values. The noise/spot in the fiber-optic system is roughly six x rays, giving a factor of 5 improvement in the low dose regime over this configuration of the lens system. Using a lower reduction ratio would improve the low dose performance of the lens system. The faster Canon lens would also give improvement due to its greater sensitivity, but would be limited somewhat in the measurement of small features by a poorer PSF, requiring a larger integration region.

Note that the smoothing that occurs in the distortion correction does not improve the S/N in the measurement of the spot intensity. The smoothing makes the spots larger, necessitating a larger integration area with an associated increase in read noise. The signal/noise can be improved with techniques such as spot profile fitting, which effectively imposes a bandpass filter on the spatial noise spectrum if the shape of the spot to be integrated is known.[26] The effect of this smoothing in correction procedures also highlights the danger of estimating a detector's noise performance by measuring the pixel-to-pixel noise in a zero dose, spatially corrected image. The reduction in the pixel-to-pixel variation will be even greater than the case above. For the correction procedure used here, the rms pixel-to-pixel variation drops by a factor of 2 to an apparent 6 e^-/read. Changes to statistics will, in general, depend on the method and the mapping used for any given detector system.

As the dose/spot increases beyond A^2 (roughly 10^3 x rays for the lens system), the $N_{\text{x-ray}}/B$ term in Eq. (3) becomes important and the DQE curve will level off. The parameter B is a measure of the quantum efficiency (or probability) of recording a signal from a given incident x ray and will be $\leqslant 1$. B will be limited by the stopping power of the phosphor (98%) and by the transmission of the window material ($\sim$95%) and aluminized mylar backing of the phosphor ($\sim$95%). Further reduction in B comes from the broad distribution in recorded signal/x ray due to the stochastic processes involved in the x-ray conversion and transmission of the light through the phosphor and optical system. The breadth of this distribution adds noise to the system. In addition, given the low mean number of quanta/x ray recorded for this detector, a broad distribution implies that there is a significant probability that zero quanta are recorded for a given x ray, reducing B yet further. For the center, where the mean recorded signal is 2 e^-/x ray, B was found to be 0.56. For the corners, with 1.3 e^-/x ray, B was found to be 0.37. The fiber-optic detector, with 7 e^-/x ray, has a considerably higher probability of recording at least 1 e^- for each x ray, giving a value of 0.8 for B.

At high dose, the DQE is seen to fall as the measurements asymptotically approach a constant accuracy (or noise:dose ratio). The fits to the DQE curves yield limiting accuracies, C, of 0.5% and 0.7% for the center and corners, respectively. Such asymptotic behavior typically results in a systematic pixel-to-pixel variation in sensitivity, referred to as fixed-pattern noise. The intensity correction procedure nominally removes this fixed pattern, but not all high frequency components are measured properly.[15] The fixed pattern intensity calibration is typically performed with a uniform field, whereas the test above (and real experiments) records images with higher spatial frequencies. Since the PSF smoothes the high frequency variation due to, say, the granular structure of the phosphor, the uniform illumination will have less variation than needed to properly correct high frequency signals. Such effects should be more pronounced with a poorer PSF, such as seen in the corners of the lens detector. Indeed, the limiting performance in the corners is lower than for the center. Interestingly, the limiting accuracy for the lens detector is better than for the fiber-optic system (C near 1%) even though the PSF for the fiber-optic detector is better. Note that the fiber-optic detector will have additional high-frequency modulation (of large magnitude) due to the fiber structure and the associated characteristic "chicken wire" pattern.

Note that the limiting accuracy, C, has been shown to depend on the size of the x-ray feature.[15] As the feature size increases, the illumination on the phosphor is more closely approximated by the uniform field illumination, yielding a more accurate intensity calibration factor. One now will be limited by the uniformity of the flood illumination used in the calibration, which can be extremely difficult to produce at levels below 0.5%. Care must also be taken to correct for sensitivity differences due to x-ray energy and angle of incidence. In practice, these effects are generally ignored, and most data being collected with CCD detectors around the world are accurate only to several percent at best. Fortu-

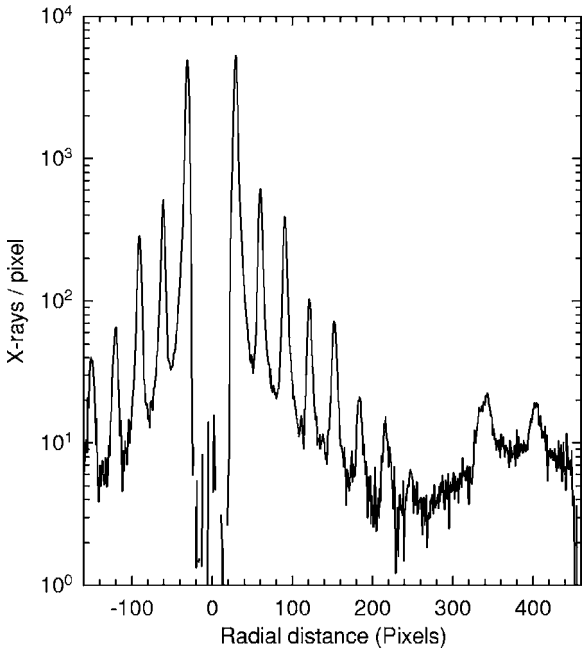

FIG. 6. Radial intensity of the small angle powder diffraction image of Fig. 5. The intensity was azimuthally averaged as a function of distance from the center of the diffraction rings. Note the intensity of the eight lamellar diffraction peaks span 3 orders of magnitude per pixel, with the signal in the 8th diffraction order (radius=250 pixels) arriving at 0.003 x rays/s per pixel. Negative values in distance correspond to pixels in the left half plane of Fig. 5 (relative to the beam), with positive values to the right of the beam. Values near pixel zero in this figure are shadowed by the beam stop.

nately, for many x-ray methods such as crystallography, the systematic errors in the recorded intensities tend to be averaged since symmetry related diffraction spots are recorded in numerous places over the face of the detector.

E. Experimental diffraction data

Figure 5 shows the small angle powder diffraction from a sample of silver stearate in the lamellar phase (lamellar spacing=4.868 nm). The sample was contained within a 0.7 mm diam glass x-ray capillary. This image is the sum of seven 200 s integrations and has been processed to remove "zingers" due to the conversion of cosmic rays or radioactive decay events in the CCD or phosphor.[22] These events occur randomly over the face of the detector at a rate of about 0.8 Hz. Dark current was subtracted using zero-dose integrations of equal time. The x-ray beam was produced using a Rigaku Ru-300 generator with a copper anode, a 0.2 mm $\times$ 2 mm point focus, and operating at 40 kV and 56 mA. The beam is focused at the detector to a spot 0.5 mm $\times$ 0.7 mm in size using a pair of crossed Franks mirrors. Beam flux was measured to be 3.4×10^7 x rays/s. Images were acquired in 2×2 binning mode with the Sigma lens set at 2.26:1 reduction. Sample to detector distance was 10.4 cm.

The observed diffraction rings from this sample span 3 orders of magnitude in intensity (Fig. 6). Diffraction from the 8th order is incident on the detector at less than 0.003 x rays/pixel/s. With this length of integration, the dark current accumulation is the dominant source of noise for these low dose signals.

IV. DISCUSSION

This article has shown that a CCD x-ray detector with good area, spatial resolution, and detective quantum efficiency can be constructed from commonly available commercial components at relatively low cost. While the sensitivity of this lens-coupled detector is less than that commonly achieved with fiber-optic couplings, it is still sufficiently high for many applications. Performance improves considerably for measurements that need higher measurement accuracy which inherently need a higher dose.

Keeping the optical surfaces clean is a major concern for long-term stability. In addition to potential problems with condensation on the optical window when operated on humid days, the hermetic enclosure will periodically need purging as water vapor and other condensables build within the detector, forming a layer on the surface of the CCD. Coatings do form on lenses over time without hermetic enclosures and will contribute to increased flare in the system and reduced sensitivity. Such a hermetic enclosure would allow further cooling of the CCD without water condensing on optical surfaces, improving the performance in long integrations.

Note that other fast aspheric lenses are available which may be more suitable in certain situations. Cameras with faster read times and universal serial bus (USB) interface are now available from several vendors. In addition, while backside illuminated chips still have the highest quantum efficiency, new technology in gate structure has improved the quantum efficiency of some frontside illuminated chips which can be obtained at somewhat lower cost.[27]

It is also interesting to consider using a CCD with a smaller imaging area in conjunction with the faster camera lenses. Since most of the distortion comes at the corners of the field, a smaller imager would be less prone to these aberrations. Of course, one would need a higher demagnification in order to image the same area at the phosphor, but this tends to move the lens closer to its designed operating regime, a range more likely to be properly corrected. The decrease in optical coupling efficiency at this higher demagnification would be offset by the larger aperture, but the optimal configuration would need further tests. One could choose to operate the CCD sensor of this article in such a mode by cropping the image to the central portion of the imaging area. By contrast, using a larger CCD would go beyond the parameters for which these 35 mm camera lenses were designed, requiring the fabrication of a custom lens to obtain good imaging quality over the entire sensor.

ACKNOWLEDGMENTS

Detector development was supported by a grant from the DOE-OBER (Grant No. DE-FG-0297ER62443). CHESS is supported by the NSF and NIH-NIGMS via Award No. DMR-0225180.

[1] H. F. Fuchs, D. Q. Wu, and B. Chu, Rev. Sci. Instrum. **61**, 712 (1990).
[2] B. Rodricks, R. Clarke, R. Smither, and A. Fontaine, Rev. Sci. Instrum. **60**, 2586 (1989).
[3] R. Clarke, Nucl. Instrum. Methods Phys. Res. A **291**, 117 (1990).
[4] B. Chu, J. Rousseau, and T. Gao, Rev. Sci. Instrum. **63**, 4000 (1992).

[5] A. Koch, Nucl. Instrum. Methods Phys. Res. A **348**, 275 (1994).
[6] E. M. Westbrook *et al.*, Proc. SPIE **4784**, 375 (2003).
[7] N. M. Allinson, J. Synchrotron Radiat. **1**, 54 (1994).
[8] W. C. Phillips, M. Stanton, A. Stewart, H. Qian, C. Ingersoll, and R. M. Sweet, J. Appl. Crystallogr. **33**, 243 (2000).
[9] E. M. Westbrook and I. Naday, Methods Enzymol. **276**, 244 (1997).
[10] S. M. Gruner, M. W. Tate, and E. F. Eikenberry, Rev. Sci. Instrum. **73**, 2815 (2002).
[11] H. W. Deckman and S. M. Gruner, Nucl. Instrum. Methods Phys. Res. A **246**, 527 (1986).
[12] E. F. Eikenberry, S. M. Gruner, and J. L. Lowrance, IEEE Trans. Nucl. Sci. **33**, 542 (1986).
[13] R. H. Templer, S. M. Gruner, and E. F. Eikenberry, Adv. Electron. Electron Phys. **74**, 275 (1988).
[14] E. F. Eikenberry, M. W. Tate, A. L. Belmonte, J. L. Lowrance, D. Bilderback, and S. M. Gruner, IEEE Trans. Nucl. Sci. **38**, 110 (1991).
[15] M. W. Tate, E. F. Eikenberry, S. L. Barna, M. E. Wall, J. L. Lowrance, and S. M. Gruner, J. Appl. Crystallogr. **28**, 196 (1995).
[16] D. J. Thiel, S. E. Ealick, M. W. Tate, S. M. Gruner, and E. F. Eikenberry, Rev. Sci. Instrum. **67**, 1 (1997).
[17] M. W. Tate, S. M. Gruner, and E. F. Eikenberry, Rev. Sci. Instrum. **68**, 47 (1997).
[18] A. D. A. Maidment and M. J. Yaffe, Phys. Med. Biol. **41**, 475 (1996).
[19] See EPAPS Document No. E-RSINAK-76-238508 for mechanical drawings for the fabrication of detector components. A direct link to this document may be found in the online article's HTML reference section. The document may also be reached via the EPAPS homepage (http://www.aip.org/pubservs/epaps.html) or from ftp.aip.org in the directory/epaps. See the EPAPS homepage for more information.
[20] S. M. Gruner, S. L. Barna, M. E. Wall, M. W. Tate, and E. F. Eikenberry, Proc. SPIE **2009**, 98 (1993).
[21] J. Janesick and T. Elliott, in *Astronomical CCD Observing and Reduction Techniques*, edited by S. B. Howell (Astronomical Society of the Pacific, San Francisco, CA, 1992), pp. 1–67.
[22] S. L. Barna, M. W. Tate, S. M. Gruner, and E. F. Eikenberry, Rev. Sci. Instrum. **70**, 2927 (1999).
[23] M. Stanton, W. C. Phillips, Y. Li, and K. Kalata, J. Appl. Crystallogr. **25**, 549 (1992).
[24] S. M. Gruner, J. R. Milch, and G. T. Reynolds, IEEE Trans. Nucl. Sci. **25**, 562 (1978).
[25] M. Stanton, Nucl. Instrum. Methods Phys. Res. A **325**, 550 (1993).
[26] M. G. Rossmann, J. Appl. Crystallogr. **12**, 225 (1979).
[27] Kodak Blue Plus CCD series, www.kodak.com/go/ccd